The Astrophysical Journal, 928:98 (10pp), 2022 April 1 https://doi.org/10.3847/1538-4357/ac590d

Three-dimensional Propagation of the Global Extreme-ultraviolet Wave Associated with a Solar Eruption on 2021 October 28

Zhenyong Hou[1,2], Hui Tian[2,3], Jing-Song Wang[1], Xiaoxin Zhang[1], Qiao Song[1], Ruisheng Zheng[4], Hechao Chen[2], Bo Chen[5], Xianyong Bai[3], Yajie Chen[2], Lingping He[5], Kefei Song[5], Peng Zhang[6], Xiuqing Hu[6], Jinping Dun[1], Weiguo Zong[1], Yongliang Song[3], Yu Xu[2], and Guangyu Tan[2]

[1] Key Laboratory of Space Weather, National Center for Space Weather, China Meteorological Administration, Beijing 100081, People's Republic of China wangjs@cma.gov.cn, xxzhang@cma.gov.cn
[2] School of Earth and Space Sciences, Peking University, Beijing, 100871, People's Republic of China; huitian@pku.edu.cn
[3] National Astronomical Observatories, Chinese Academy of Sciences, Beijing, 100012, People's Republic of China
[4] School of Space Science and Physics, Institute of Space Sciences, Shandong University, Weihai, Shandong, 264209, People's Republic of China
[5] Changchun Institute of Optics, Fine Mechanics and Physics, Chinese Academy of Sciences, Changchun 130033, People's Republic of China
[6] Innovation Center for Fengyun Meteorological Satellite, National Satellite Meteorological Center, China Meteorological Administration, Beijing 100081, People's Republic of China

Received 2022 January 5; revised 2022 February 25; accepted 2022 February 25; published 2022 March 30

Abstract

We present a case study for the global extreme-ultraviolet (EUV) wave and its chromospheric counterpart the *Moreton-Ramsey Wave* associated with the second X-class flare in Solar Cycle 25 and a halo coronal mass ejection (CME). The EUV wave was observed in the Hα and EUV passbands with different characteristic temperatures. In the 171 Å and 193/195 Å images, the wave propagates circularly with an initial velocity of 600–720 km s^{-1} and a deceleration of 110–320 m s^{-2}. The local coronal plasma is heated from $\log(T/K) \approx 5.9$ to $\log(T/K) \approx 6.2$ during the passage of the wave front. The Hα and 304 Å images also reveal signatures of wave propagation with a velocity of 310–540 km s^{-1}. With multiwavelength and dual-perspective observations, we found that the wave front likely propagates forwardly inclined to the solar surface with a tilt angle of ∼53°.2. Our results suggest that this EUV wave is a fast-mode magnetohydrodynamic wave or shock driven by the expansion of the associated CME, whose wave front is likely a dome-shaped structure that could impact the upper chromosphere, transition region, and corona.

Unified Astronomy Thesaurus concepts: Solar activity (1475); Solar coronal waves (1995); Solar coronal mass ejections (310)

Supporting material: animations

1. Introduction

Over the past two decades, coronal wave-like phenomena, i.e., extreme-ultraviolet (EUV) waves have been extensively studied (Liu & Ofman 2014; Chen 2016). These EUV waves usually appear as propagating bright or dark fronts in coronal EUV images (e.g., Thompson et al. 1999; Wills-Davey & Thompson 1999; Thompson & Myers 2009; Liu et al. 2010; Chen & Wu 2011; Shen & Liu 2012a; Tian et al. 2012; Shen et al. 2014b; Ying et al. 2018; Shen et al. 2018). They are sometimes simultaneously observed with the Moreton-Ramsey Waves (Warmuth et al. 2001; Eto et al. 2002; Okamoto et al. 2004; Shen & Liu 2012a; Asai et al. 2012; Shen et al. 2019; Long et al. 2019), which are chromospheric waves observed in Hα images (Moreton 1960; Moreton & Ramsey 1960; Smith & Harvey 1971; Shibata et al. 2011). The EUV waves are often associated with large-scale energetic eruptions, e.g., coronal mass ejections (CMEs) and flares (Biesecker et al. 2002; Nitta et al. 2013; Liu et al. 2018). However, small-scale events such as surges, jets, minifilaments, and mini-CMEs may also drive EUV waves (e.g., Zheng et al. 2011, 2012a, 2012b, 2012c, 2012d, 2013a, 2013b; Shen et al. 2017).

The large-scale EUV waves have often been interpreted as fast-mode MHD waves (Thompson et al. 1999; Wang 2000; Warmuth et al. 2001; Ofman & Thompson 2002; Li et al. 2012; Liu et al. 2018) driven by CME expansion (Shen & Liu 2012b; Asai et al. 2012; Liu et al. 2012; Shen et al. 2013, 2018) and often followed by nonwave components due to the CME-caused magnetic field reconfiguration (Chen et al. 2002, 2005; Shen & Liu 2012a; Downs et al. 2012; Liu et al. 2012). The EUV waves generally propagate as a single wave front, while sometimes appearing in the form of multiple wave fronts (Liu et al. 2012; Shen et al. 2019). Their propagating velocities are measured to be 50–700 km s^{-1} with typical values of 200–400 km s^{-1} (Thompson & Myers 2009) from the observations of the Extreme-ultraviolet Imaging Telescope (Delaboudinière et al. 1995) on board the Solar and Heliospheric Observatory (SOHO; Moses et al. 1997; Thompson et al. 1998), and 200–1500 km s^{-1} with an averaged value of 644 km s^{-1} (Nitta et al. 2013) from the high-resolution observations with the Atmospheric Imaging Assembly (AIA; Lemen et al. 2012) on board the Solar Dynamics Observatory (SDO; Pesnell et al. 2012). Previous studies have shown that the EUV waves often experience a deceleration process with a deceleration of an order of several hundred m s^{-2} (e.g., Warmuth et al. 2001; Vršnak et al. 2002, 2005; Veronig et al. 2008, 2011; Nitta et al. 2013). As the EUV waves propagate, they could interact with coronal structures. For instance, the wave fronts could not only exhibit reflections

(Li et al. 2012; Olmedo et al. 2012; Shen et al. 2013; Yang et al. 2013; Liu et al. 2018; Zhou et al. 2021b), transmissions (Liu et al. 2012; Olmedo et al. 2012; Shen et al. 2013; Liu et al. 2018) and refractions (Thompson et al. 2000; Shen & Liu 2012b; Shen et al. 2013) but also result in oscillations of coronal loops (Shen & Liu 2012b; Liu et al. 2012; Zheng et al. 2013b) and filaments (Okamoto et al. 2004; Asai et al. 2012; Shen et al. 2014a, 2014b, 2017). EUV waves are often accompanied by quasi-periodic fast-mode propagating wave trains (Liu & Ofman 2014; Shen et al. 2022; Duan et al. 2022). Signatures of coronal heating have also been found near wave fronts (Wills-Davey & Thompson 1999; Downs et al. 2012; Liu et al. 2018).

Limb observations have shown that an EUV wave does have a dome-shaped wave front (Veronig et al. 2010; Li et al. 2012; Selwa et al. 2012; Liu et al. 2012; Shen et al. 2014a; Zhou et al. 2021a). In the studies of Veronig et al. (2010), Li et al. (2012), and Shen et al. (2014a), the upward expansions of wave fronts were found to be faster than the lateral expansions. With AIA observations, Liu et al. (2012) studied an off-limb EUV wave with an initial height of 110 Mm driven by a dome-shaped CME front and found that the wave front propagates forwardly inclined toward the surface of the Sun (Liu et al. 2018).

With stereoscopic observations in dual perspectives and multipassbands, here we report one global EUV wave observed at the beginning of Solar Cycle 25, and investigate the three-dimensional (3D) propagation of the wave front as well as its impact on the coronal plasma temperature. We describe our observations in Section 2, present the analysis results in Section 3, discuss the results in Section 4, and summarize our findings in Section 5.

2. Observations

The global EUV wave of interest occurred on 2021 October 28, was simultaneously observed by AIA on board SDO, the Extreme-Ultraviolet Imager (EUVI; Howard et al. 2008) on board the Solar Terrestrial Relations Observatory (STEREO; Kaiser et al. 2008), the Solar X-ray Extreme Ultraviolet Imager (X-EUVI) on board the Fengyun-3E Satellite (FY-3E; Zhang et al. 2021), and the Global Oscillation Network Group (GONG; Harvey et al. 2011). From the Earth's view, the full-disk EUV images taken by AIA and X-EUVI revealed the propagations of the EUV wave from the top-down view. Images of all the AIA EUV passbands, with a 12 s cadence and a $\sim 0''.6$ pixel size, were used in this study. Different from the AIA 193 Å passband centered at 193 Å, the EUV image taken by X-EUVI on board FY-3E in an early morning orbit is centered at 195.5 Å with a bandwidth of 7.5 Å. It is the only EUV passband of the X-EUVI instrument. The preprocessing procedure of the X-EUVI 195 Å image is described in Q. Song et al. (2022a, in preparation). The X-EUVI 195 Å image has a cadence of $\sim$14 s and a pixel size of $\sim 2''.5$. The X-EUVI data will be released to the community after the satellite on-orbit commission test is completed. We also analyzed the Hα images provided by GONG to investigate the chromospheric counterpart of the EUV wave. The Hα images with a cadence of 60 s and a pixel size of $1''.07$ were taken with a filter centered at 6562.8 Å.

In the meantime, on the western side of the Earth, STEREO-Ahead was separated about $37°.5$ from the Earth-Sun line. The 195 and 304 Å images taken by STEREO-Ahead/EUVI revealed the propagation of the EUV wave from the edge-on view. The pixel size of these images is $1''.58$, and the cadence is $\sim$2.5 minutes.

Since the X-EUVI 195 Å and the AIA 193 Å images have similar temperature responses, we aligned them through a linear Pearson correlation. For aligning the Hα images and the AIA images, the sunspot and its surrounding plage region within AR 12887 in the Hα and AIA 1600 Å images were used as the reference features.

3. Results

Figure 1 presents an overview of the solar corona at 15:10 UT in the AIA 193 Å and X-EUVI 195 Å passbands, which includes four active regions (ARs), a polar coronal hole, and the rest quiet-Sun regions. Among them, NOAA AR 12887 was located in the southern hemisphere and close to AR 12889. AR 12887 was very active around October 28, generating a global EUV wave that we study here, as well as its associated X1.0 flare and halo CME. The X1.0 flare started and peaked at 15:17 UT and 15:35 UT, respectively. It is the first X-class flare that occurred around the disk center in Solar Cycle 25, and its eruption mechanism is investigated by Q. Song et al. (2022b, in preparation). The global EUV wave appeared at $\sim$15:28 UT and quickly propagated to the surrounding areas, affecting almost the entire front side of the Sun. From the coronagraph images taken by SOHO/LASCO, we can see an associated halo CME that first appeared around 15:53 UT.

The stereoscopic observations of multiple spacecraft with high spatial and temporal resolutions revealed the evolution of this global EUV wave very well, allowing us to investigate its 3D propagation and its impact on the coronal plasma.

3.1. Overview of the EUV Wave

The morphological evolution of the remarkable global EUV wave from the top-down view is shown in Figure 2 and the associated animation. To highlight the wave fronts, we drew colored dashed lines outlining the outer edge of wave fronts in the AIA 193 Å, 171 Å, 304 Å, and Hα running-difference images (2 minutes separation). The colored dashed lines in Figure 2 were visually determined. The EUV wave first appeared around 15:28 UT and propagated outwards as a circular wave front, which was clearly detected in the 193 and 171 Å passbands. Meanwhile, a dimming region followed behind the EUV wave, evolving from a small region to a ring-shaped region, as marked by the red arrows in Figure 2(a1). For a detailed evolution of the EUV wave and the dimming region, we refer to the associated animation of Figure 2. The 193 Å passband reveals the initial stage of the wave front propagation most clearly (see the black dashed line in Figure 2(a1)), while the 171 Å, 304 Å, and Hα passbands show weak wave signatures. As the northern part of the EUV wave continues to propagate, its southern part is hard to see. In addition, as shown in Figure 2 and the associated animation, the wave front interacts with various coronal structures, resulting in not only the commonly observed reflections/refractions but also emission perturbations such as brightening in 193 Å and darkening in 171 Å.

We also present the morphological evolution of the EUV wave observed by the EUVI 195 and 304 Å passbands from the edge-on view in Figure 3 and the associated animation. The wave fronts in 195 Å and 304 Å are also highlighted by the colored dashed lines in Figure 3. The animation reveals that the

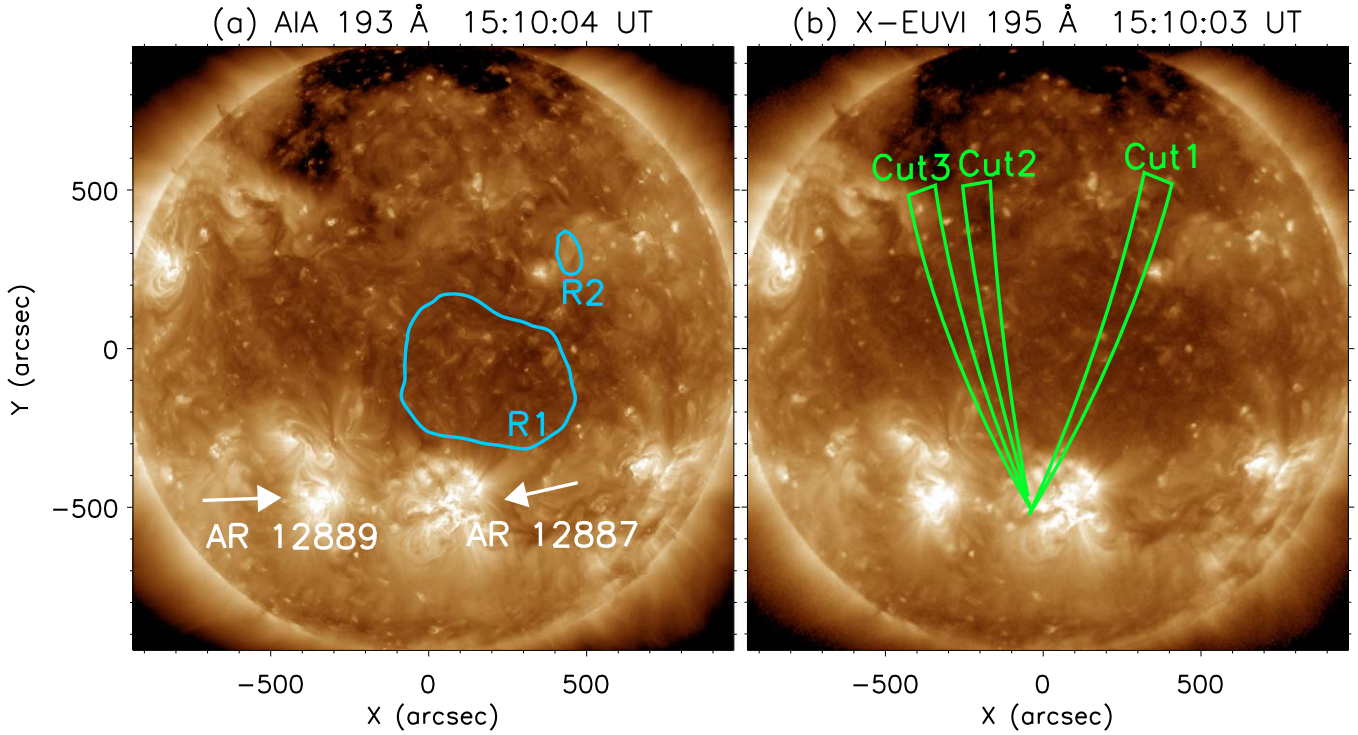

Figure 1. Overview of the solar corona before the flare in the AIA 193 Å (a) and X-EUVI 195 Å (b) images. In (a), the white arrows indicate the locations of AR 12887 and AR 12889, and the cyan contours outline two regions used to obtain the normalized intensity variations at the AIA EUV passbands shown in Figure 7. In (b), the green lines represent three sector cuts used to obtain the time-distance diagrams shown in Figure 4.

wave front appears as a dome-like structure in the EUVI 195 Å image around 15:30 UT and evolves globally. The wave front in 304 Å experiences an evolution similar to that in 195 Å.

Notably, the northern part of the wave front is more evident than its southern part in Figures 2 and 3 (and their associated animations). Particularly, only the northern wave front was observed by the AIA 304 Å and Hα passbands in the form of arc-shaped structures. Therefore, we focus on the propagation of the northern part of this EUV wave.

3.2. 3D Propagation of the EUV Wave

We have defined three sector cuts originating from the eruption center and perpendicular to the wave fronts, as indicated by the green triangles in Figure 1(b), to obtain time-distance diagrams. Figure 4 shows the time-distance diagrams derived from the running-difference images of the X-EUVI 195 Å, AIA 193 Å, 171 Å, 304 Å, and Hα passbands, which could reflect the propagation of the EUV wave in the plane of the sky from the top-down view. The distances were estimated along the sector cuts by considering the curvature of the solar surface. In the time-distance diagrams, the colored dotted lines mark the propagating tracks of the outer edges of the wave fronts in different images, which were visually determined.

The propagations of the wave fronts are manifested as evident, wide stripes in the X-EUVI 195 Å, AIA 193 Å, and 171 Å images and weak, narrow ones in the AIA 304 Å and Hα images. From Figure 4, we can see that the propagating signatures appear about 150 Mm away from the eruption center. The wave front appears to be bright in 195/193 Å and dark in 171 Å. As shown in the first and second rows of Figure 4, the overplotted black dotted lines were both obtained from the AIA 193 Å time-distance diagrams, revealing that the propagating tracks in 195 and 193 Å coincide well with each other.

We further plotted the propagating tracks of the wave fronts along Cut 1, Cut 2, and Cut 3 in Figure 5. To quantitatively determine the average velocities and accelerations, we applied linear fits and quadratic polynomial fits to the propagating tracks, respectively. The resulting velocities and accelerations for different sector cuts and passbands are also shown in Figure 5. The propagating tracks in the Hα time-distance diagrams are too weak for an accurate calculation of the acceleration. It can be seen that the EUV wave fronts propagate at velocities of 420–510 km s^{-1} and decelerations of 110–320 m s^{-2} in the AIA 193 Å and 171 Å passbands. We also calculated the propagating velocity of the EUV wave during its initial propagation stage during 15:28–15:32 UT and obtained a velocity of 600–720 km s^{-1}. Our results are consistent with the previous studies by Warmuth & Mann (2011) and Muhr et al. (2014), in which they found that some events with fast initial velocities (>300 km s^{-1}) show distinct deceleration (several hundred m s^{-2}) during their propagations. On the other hand, the chromospheric counterpart of the EUV wave propagates in the Hα passband at a velocity of 310–540 km s^{-1}, which is similar to that in the AIA 304 Å passband.

We also found that the propagating tracks in 193 Å significantly precede those in the other passbands with lower temperatures such as 304 Å and Hα (see the colored tracks in Figure 5). Though not explicitly mentioned in Asai et al. (2012), we noticed a similar behavior in their event, in which the EUV wave front slightly preceded the Hα wave front. This indicates that the wave fronts with different temperatures propagate to different distances within the same period of time, i.e., the wave front with a higher temperature propagated ahead of those with lower temperatures. From Figure 5, we calculated

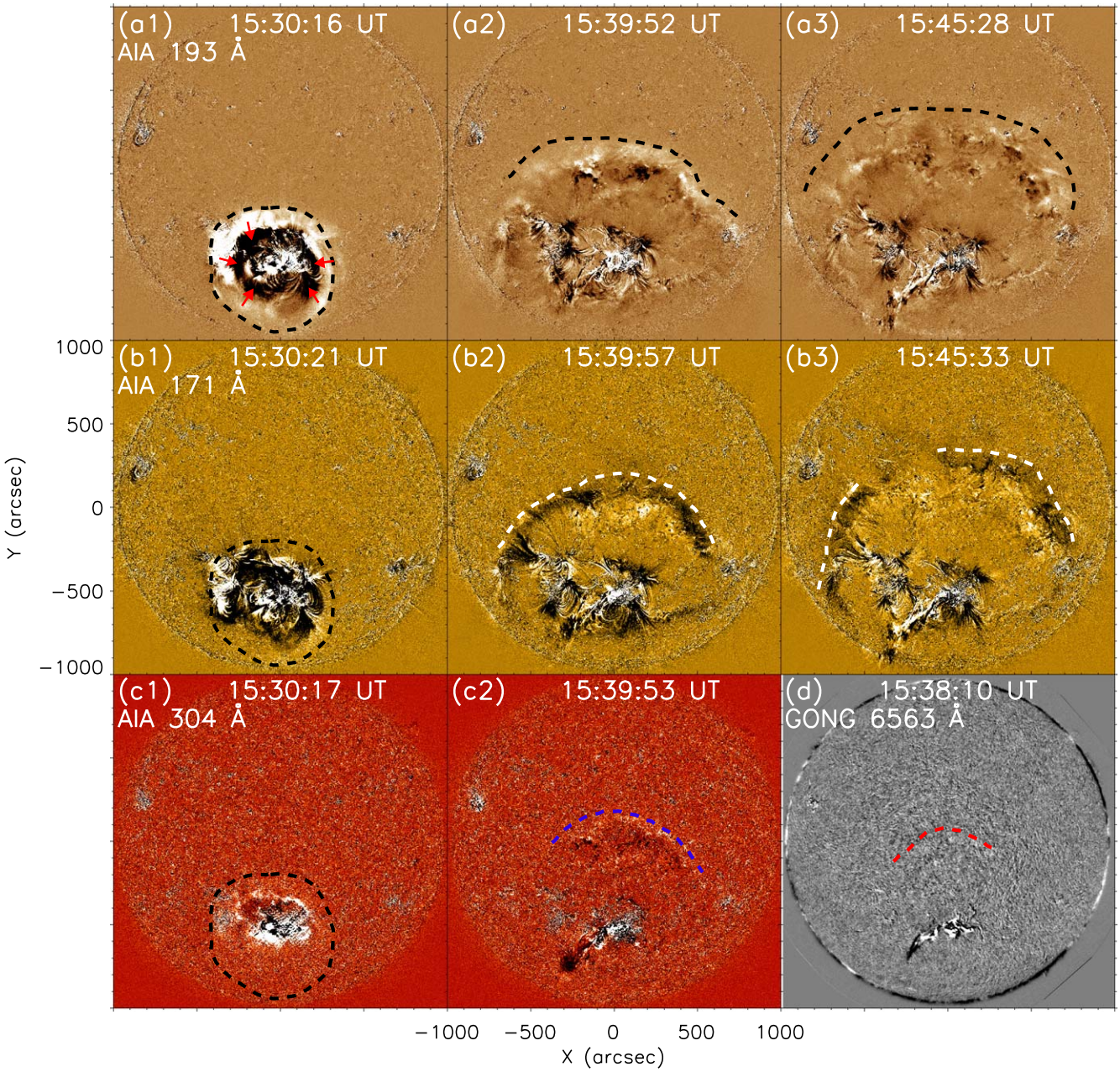

Figure 2. Propagation of the EUV wave from the top-down view. The images are the running-difference images of the AIA 193 Å, 171,Å, 304 Å, and GONG Hα 6563 Å passbands. The black, white, blue, and red dashed lines outline the wave fronts obtained from the AIA 193 Å, 171 Å, 304 Å, and Hα running-difference images, respectively. An animation of this figure is available, showing the propagation of the EUV wave from the top-down view. It covers a duration of ∼43 minutes from 15:12 UT to 15:55 UT on 2021 October 28.

(An animation of this figure is available.)

the differences of the plane-of-sky distances in the 193 Å and 304 Å passbands for Cuts 1–3 in the time periods of 15:32–15:38 UT, which are 43.9 ± 7.5 Mm, 55.2 ± 21.1 Mm, and 51.5 ± 23.4 Mm, respectively. We take the averaged value 50.5 Mm for further analysis.

As mentioned above, the EUV wave was observed in dual perspectives, allowing us to derive the height difference between the wave fronts with different temperatures (e.g., 195 Å from FY-3E/X-EUVI and STEREO-Ahead/EUVI; 304 Å from SDO/AIA and STEREO-Ahead/EUVI). Using the stereoscopic observations, we reconstructed the 3D structures of the wave fronts in the 195 and 304 Å passbands, and derived the heights of the wave fronts in these two passbands through the *SSW* procedure ("scc_measure.pro"). As shown in Figure 6, we measured the wave front heights at three different times in the 195 and 304 Å passbands by choosing several points (marked by the cyan plus symbols) along the outer edges of the wave fronts. The derived heights of the wave fronts in 304 Å are 3.5 ± 1.3 Mm (T1), 3.6 ± 2.0 Mm (T2), and 4.2 ± 1.7 Mm (T3), while the heights in 195 Å have been estimated to be 37.2 ± 17.9 Mm (T1), 89.3 ± 44.0 Mm (T2), and 87.0 ± 41.2 Mm (T3). The wave front heights in 195 Å are consistent with those reported by Patsourakos et al. (2009), Kienreich et al. (2009), Liu et al. (2012), and Shen & Liu (2012b). Based on these results, we calculated the average height differences of the wave fronts between the 195 Å and

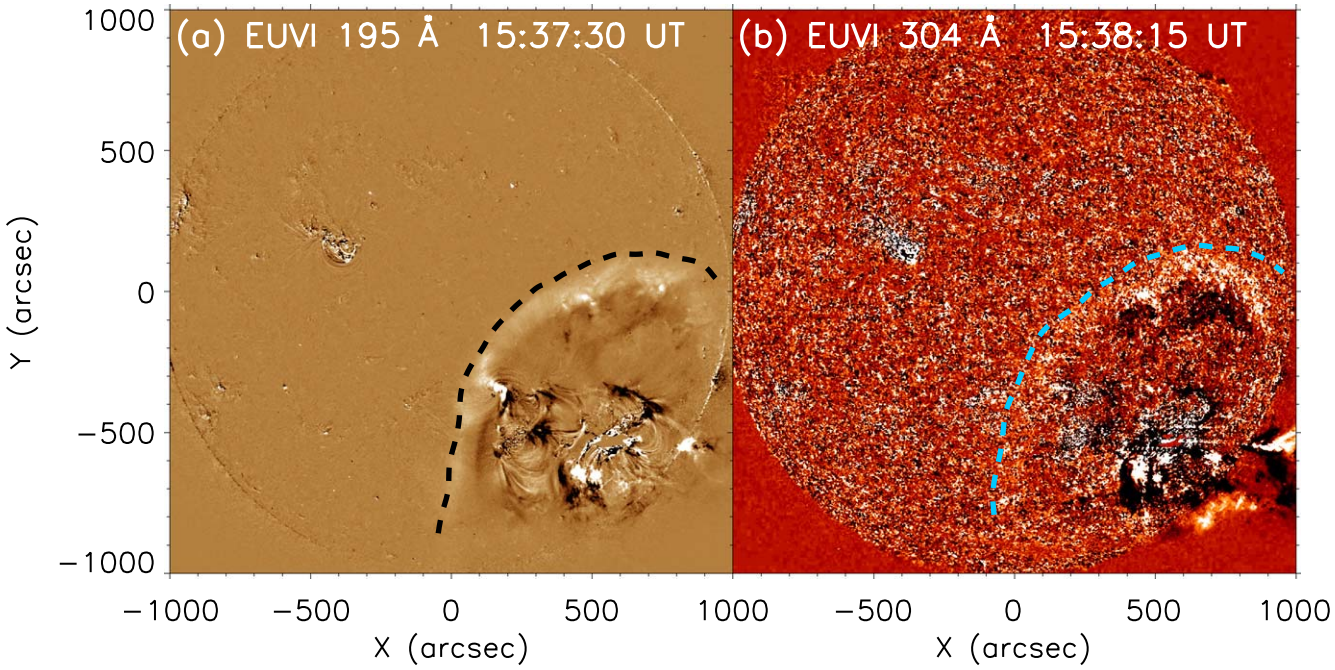

Figure 3. Propagation of the EUV wave from the edge-on view. The black and cyan dashed lines outline the wave fronts obtained from the EUVI 195 Å (a) and 304 Å (b) running-difference images. An animation of this figure is available, showing the propagation of the EUV wave from the edge-on view. It covers a duration of ∼53 min from 15:12 UT to 16:05 UT on 2021 October 28.

(An animation of this figure is available.)

304 Å passbands, which are 33.8 Mm, 85.7 Mm, and 82.8 Mm at T1, T2, and T3, respectively. We take the average value 67.4 Mm as the distance between the wave fronts in the two passbands in the radial direction.

This, combined with the difference in the plane-of-sky distances of the wave fronts between the two passbands, indicates that the wave front propagated forwardly inclined to the solar surface with an averaged tilt angle of arctan (67.4/50.5) = 53°.2 in the time period of 15:32–15:38 UT.

3.3. Heating of the Coronal Plasma by the EUV Wave

In Sections 3.1 and 3.2, we detected an opposite intensity change between the 193/195 Å and 171 Å passbands, as shown in Figure 2 and Figure 4. We have analyzed the thermal response of the corona plasma to the EUV wave in detail, and shown the results in Figure 7.

The top and middle rows of Figure 7 present normalized light curves in different AIA passbands for a quiet-Sun region ("R1") and a loop footpoint region ("R2") marked by the cyan contours in Figure 1(a). These two regions were impacted by the EUV wave. When the EUV wave reaches "R1" around 15:30 UT, the intensities in 193 Å, 211 Å, 335 Å, and 94 Å all increase substantially, while the 171 Å intensity decreases. After 15:40 UT, the 193/211/335/94 Å intensities begin to decrease and the 171 Å intensity increases. Since the temperature responses of the 193 Å and 211 Å passbands peak at higher temperatures compared to the 171 Å passband, this result likely suggests a plasma heating and cooling cycle in the corona (e.g., Wills-Davey & Thompson 1999; Li et al. 2012; Downs et al. 2012; Liu et al. 2012, 2018), in which the plasma in the corona experiences heating from $\log(T/K) \approx 5.9$ to $\log(T/K) \approx 6.2$ before cooling. The 304 Å intensity also increases as the EUV wave reaches it, which might be related to the compression of the transition region plasma.

To examine the emission changes at different temperatures caused by the EUV wave, we also performed a differential emission measure (DEM) analysis (Cheung et al. 2015; Su et al. 2018; Xue et al. 2020; Samanta et al. 2021) for "R1". The result is shown in Figure 7(b). We can see that the DEM around $\log(T/K) \approx 6.2$ increases after 15:30 UT and decreases after 15:40 UT. Simultaneously, the DEM around $\log(T/K) \approx 5.9$ shows an opposite change, indicating the plasma heating and subsequent cooling process. When the EUV wave reaches "R2" around 15:40 UT, we see similar results, as shown in Figures 7(c) and (d). This means that the local plasma at the loop footpoint region "R2" may have also been heated from $\log(T/K) \approx 5.9$ to $\log(T/K) \approx 6.2$ by the EUV wave.

We further present the time-distance diagrams along Cut 2 from the running-difference EM maps at four temperatures ($\log(T/K) = 5.9$, 6.0, 6.1, and 6.2) in Figure 7(e1)–(e4), respectively. We see a dark propagating track of the wave front at the temperatures of $\log(T/K) = 5.9$ and 6.0, and a bright propagating track at the temperature of $\log(T/K) = 6.2$, indicating plasma heating from $\log(T/K) \approx 5.9$ to $\log(T/K) \approx 6.2$.

To determine whether the heating and cooling processes associated with the observed wave fronts are adiabatic, we examined the adiabatic relation, i.e., $T\rho^{\gamma-1} = \text{Const}$, which gives $\delta T/T = (\gamma - 1)\delta\rho/\rho$. Here $\delta T/T$ and $\delta\rho/\rho$ represent the relative changes of temperature and density, respectively. The adiabatic index γ is 5/3. Through a DEM analysis, Downs et al. (2021) found that perturbations of the density and temperature in an observed wave front are 24% and 15%, respectively, consistent with an adiabatic process. Here we took the wave front height (∼87 Mm at 15:38 UT) in 195 Å as a rough estimation of the line-of-sight integration length, and calculated the density in region R2. We also estimated the temperature and its variation by integrating the DEM over the temperature range of $\log(T/K) = 5.5$–6.8. The variations of the

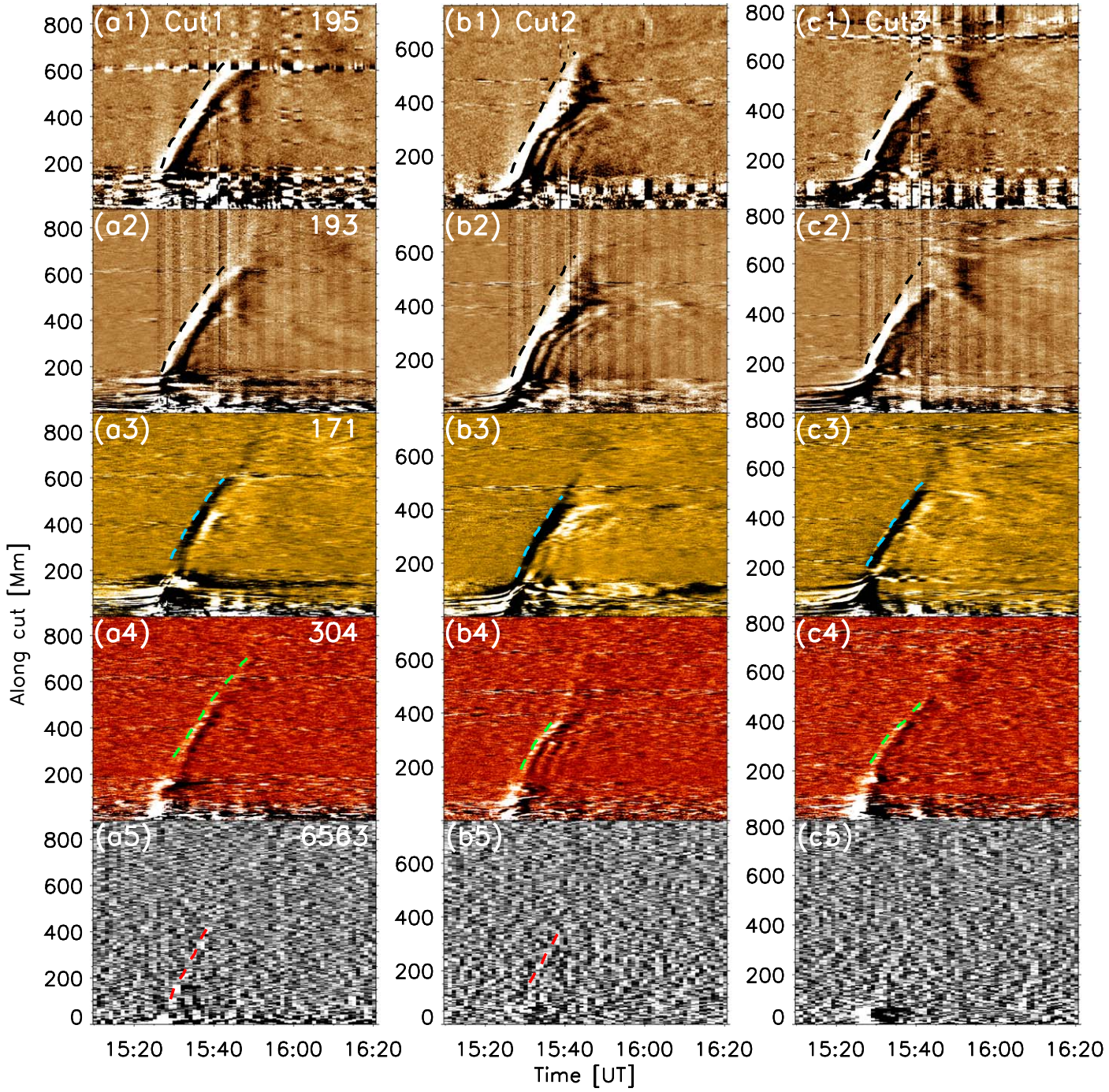

Figure 4. Time-distance diagrams showing the propagation properties of the EUV wave, as obtained from the X-EUVI 195 Å, AIA 193 Å, 171 Å, 304 Å, and GONG Hα 6563 Å running-difference images. For the AIA 193 Å, 171 Å, 304 Å, and GONG Hα 6563 Å time-distance diagrams, the dashed lines in different colors represent the tracks of the propagating wave fronts. The dashed lines overplotted in the X-EUVI 195 Å time-distance diagrams are the same as those in the AIA 193 Å time-distance diagrams.

density and temperature after the passage of the wave front were estimated to be 3%–4.5% and 2%–2.8%, respectively, which are also consistent with an adiabatic process. However, this conclusion may need to be taken with caution as the density and temperature estimations are likely subject to large uncertainties.

4. Discussion

In the last twenty years, the EUV waves have been extensively studied. Despite intensive debates on the nature of the EUV waves, in recent years more and more researchers tend to interpret these waves by a "hybrid model," in which an outer wave component is likely a fast-mode MHD wave driven by the CME expansion, and an inner nonwave component is caused by the magnetic field reconfiguration during the CME eruption (Downs et al. 2012; Liu et al. 2012; Liu & Ofman 2014; Chen 2016). The primary EUV wave that we studied is accompanied by an X1.0 flare and a halo CME. It originates from a distance of ~150 Mm away from the eruption center, where the accompanying dimming region stops

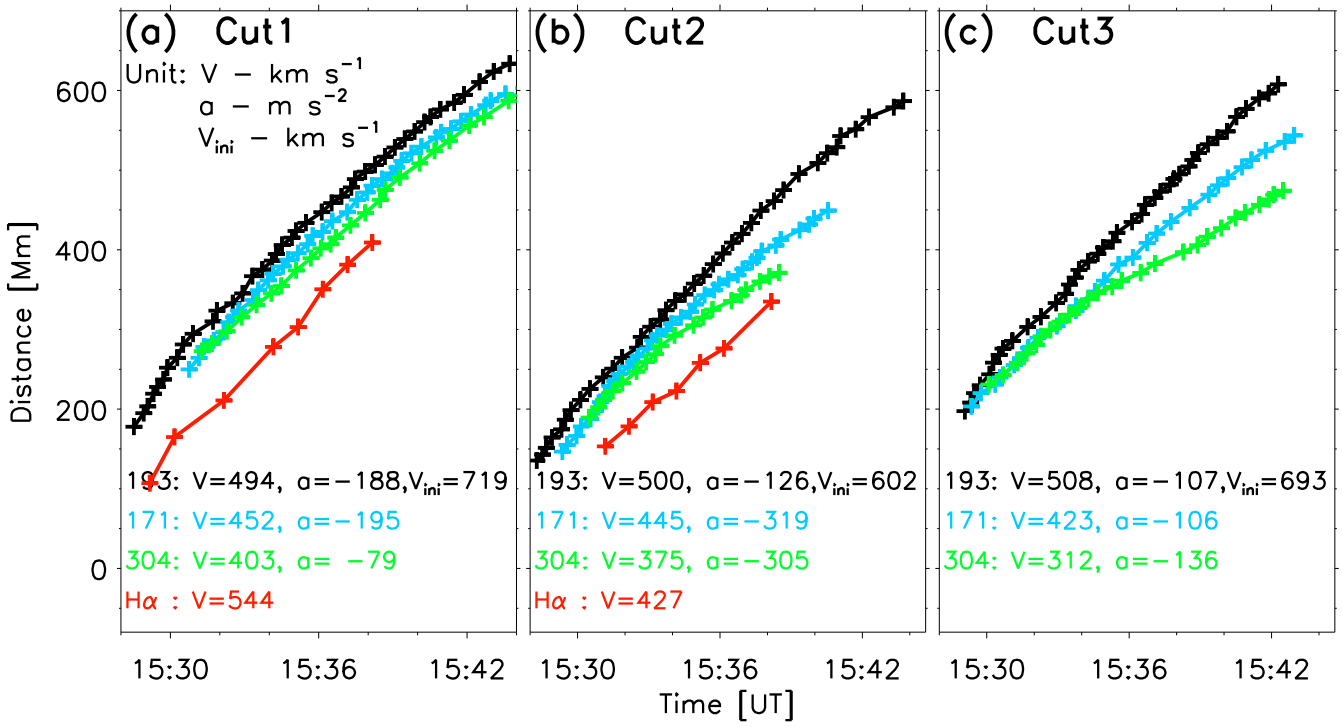

Figure 5. Tracks of the propagating wave fronts. The tracks in the AIA 193 Å, 171 Å, 304 Å, and GONG Hα 6563 Å passbands are the dotted lines in Figure 4. In each panel, "V" and "V_{ini}" indicate the averaged and initial velocities of the EUV wave in km s^{-1} as derived from linear fits to the whole and starts of tracks, respectively, while "a" indicates the accelerations of the EUV wave in m s^{-2} as derived from quadratic polynomial fits to the whole tracks.

expanding, and the wave front continues to propagate with an initial velocity of 600–720 km s^{-1} and a significant deceleration of 110–320 m s^{-2}. The initial velocity is larger than the local sound speed (∼150 km s^{-1}), and possibly also larger than the coronal Alfvén speed (200–400 km s^{-1}, Gopalswamy et al. 2012). These indicate that the EUV wave is likely a nonlinear fast-mode MHD wave or shock driven by the CME expansion (Asai et al. 2012; Shen & Liu 2012b; Liu et al. 2012; Shen et al. 2013, 2018). Assuming that this EUV wave decays to an ordinary fast-mode wave, its final velocity can be taken as a proxy for the fast-mode speed. Then, the fast-mode Mach number is estimated to be 1.52–1.82 for this event by dividing the initial velocity by the final one (estimated to be 380–440 km s^{-1}).

The EUV wave is likely a 3D structure propagating along the solar surface with a fast-mode speed. The wave fronts observed in the 193 Å and 171 Å passbands are the line-of-sight integrations projected on the solar disk at the temperature of 1.5 MK and 1 MK, respectively. As reported by Warmuth & Mann (2005) and Downs et al. (2021), the fast-mode speed increases with height and leads to the wave front at larger heights having a faster apparent motion on the solar surface. Our result that the wave front seen at 193 Å propagates faster than the one in 171 Å is consistent with this when we consider the effect that temperature has on the observability of the wave fronts. The densities of plasma at various temperatures show a different fall-off with height due to the different hydrostatic scale height. Thus, emission of the cooler plasma at 171 Å is more concentrated at lower heights than emission at 193 Å, and the same holds for the observed wave fronts. Therefore, the different propagation speeds determined from the locations of the wave fronts in 193 and 171 Å might well be a result of this hydrostatic weighting bias. For 304 Å, the presence of emission lines with different formation temperatures in the 304 Å passband makes it hard to determine the dominated emission for the wave signatures. However, we found that the wave front has a chromospheric height and is preceded by and lower than the 193 Å wave front, indicating that the 304 Å wave front is likely dominated by the He II line. For the chromospheric counterpart Moreton-Ramsey Wave, the wave front signature is dominated by the chromospheric Hα line and also clearly preceded by the 193 Å wave front. Then, the difference of the propagating speeds between the coronal and chromospheric/transition region wave fronts would be also an effect of temperature.

Shen & Liu (2012a) reported an EUV wave simultaneously observed in the 1600/1700 Å, Hα, 193 Å, and 211 Å filters, covering a broad temperature range from the photosphere to the low corona. They found that the EUV wave had similar initial propagating velocities in the photospheric and coronal passbands, and suggested that the coronal wave and its photospheric/chromospheric counterparts had a common origin. We also observed a chromospheric counterpart of the EUV wave in the Hα images, indicating that the EUV wave is accompanied by a Moreton-Ramsey Wave. However, no wave signature appeared in the 1600/1700 Å images from SDO/AIA. This implies that the EUV wave in our study may have affected the upper chromosphere but not deeper in the atmosphere.

Several previous observations have shown that EUV waves could be detected in the 304 Å passband (Liu et al. 2010; Long et al. 2011; Shen & Liu 2012a, 2012b; Ying et al. 2018; Long et al. 2019). In quiet-Sun regions and ARs, the AIA 304 Å passband is dominated by two He II 303.8 Å lines, which are

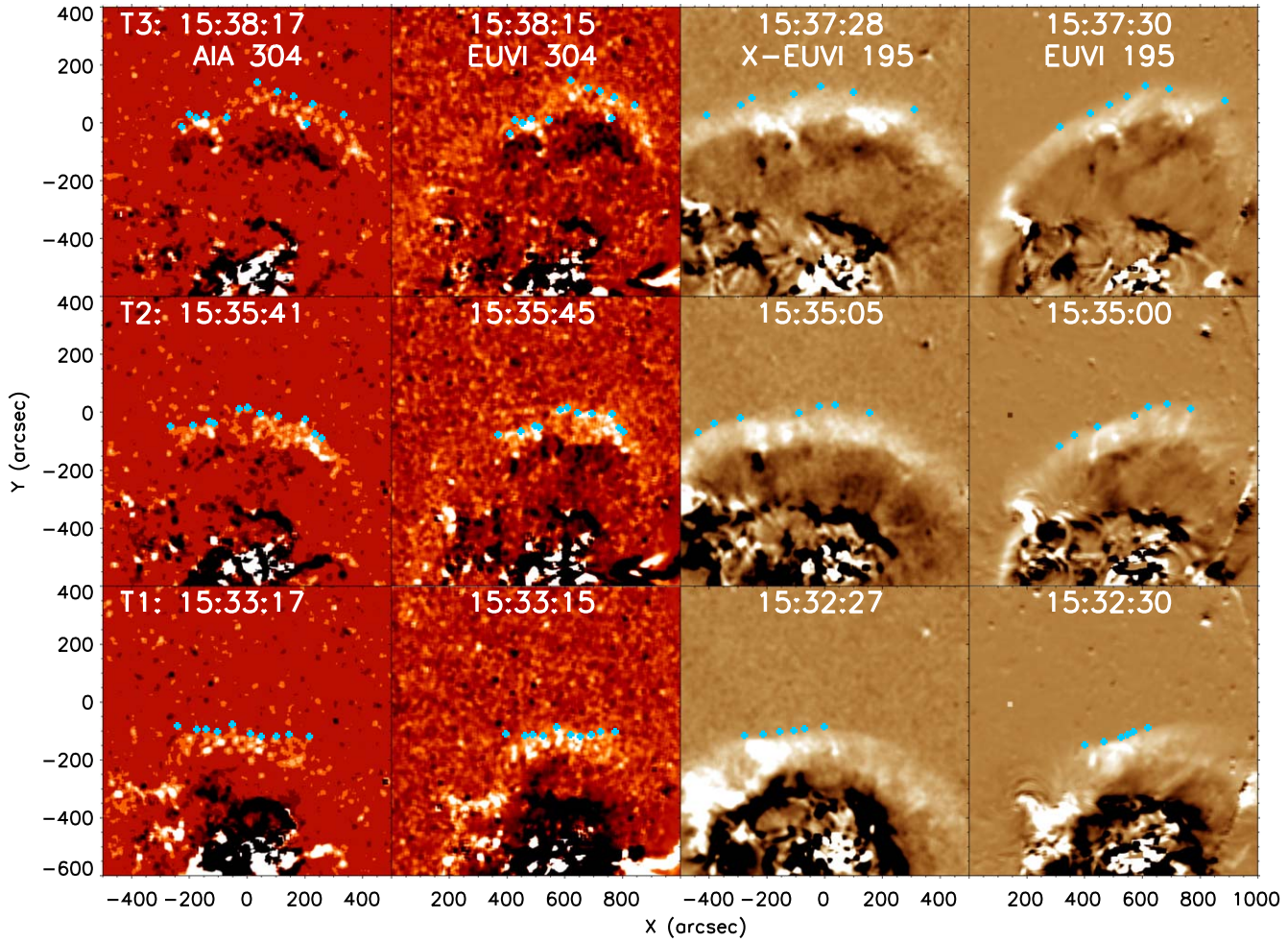

Figure 6. Triangulations of the wave fronts in the 304 and 195 Å passbands. From bottom to top, three times ∼15:33 UT, ∼15:35 UT, and ∼15:38 UT are defined as T1, T2, and T3. The cyan symbols are selected to indicate locations of the wave fronts.

formed in the transition region at a temperature of $\log(T/K) \approx 4.7$, but a coronal line of Si XI 303.33 Å at the temperature of $\log(T/K) \approx 6.2$ could also make an important contribution to the 304 Å passband in some cases (O'Dwyer et al. 2010). Shen & Liu (2012a) found that the propagation of an EUV wave in the 304 Å images was similar to that in the 193 Å passband and suggested that the wave front in the 304 Å passband was the manifestation of the contribution of the coronal Si XI line rather than the transition region He II line. However, in our event, we found that the 304 Å wave front with a chromospheric height is preceded by and lower than the 193/195 Å wave front, suggesting that the 304 Å wave front is likely dominated by the He II line. Also, the 304 Å wave front clearly precedes the Hα wave front, suggesting that the 304 Å passband may be used to reveal the link between the coronal EUV wave and the chromospheric Moreton-Ramsey Wave.

For the EUV waves, dome-like wave fronts have been reported by some authors (Veronig et al. 2010; Li et al. 2012; Selwa et al. 2012; Liu et al. 2012; Shen et al. 2014a; Zhou et al. 2021a). Veronig et al. (2010), Li et al. (2012), and Shen et al. (2014a) found that the upward expansions of their studied wave fronts were faster than the lateral expansions of the wave fronts. With AIA observations, Liu et al. (2012) analyzed an off-limb EUV wave driven by a dome-shaped CME front, and suggested that its wave front propagated forwardly inclined to the solar surface (Liu et al. 2018). Similarly, in our event, the propagating tracks in the warm passbands (e.g., 193 Å and 195 Å) precede those in the cool passbands (e.g., 304 Å) by ∼36.4 Mm. Meanwhile, we found the wave front in the 195 Å passband ∼67.4 Mm higher than that in the 304 Å passband from dual-perspective and multipassband observations. Based on these findings, we suggest that the propagating wave front appears to be a dome-like structure, propagating forwardly inclined toward the solar surface with an averaged tilt angle of ∼53°.2 in the time period of 15:32–15:38 UT. This is consistent with the findings of Liu et al. (2012), in which the slit angle of the wave front near the flare site appeared to decrease with decreasing height, ranging from 73° at 72 Mm to 48° at the coronal base. Also, it has been reported that wave fronts of the EUV waves tend to get increasingly tilted during their propagations (Hudson et al. 2003; Patsourakos & Vourlidas 2009; Kienreich et al. 2009; Liu et al. 2012) due to the increase of fast-mode speed with height in the low corona (Warmuth & Mann 2005).

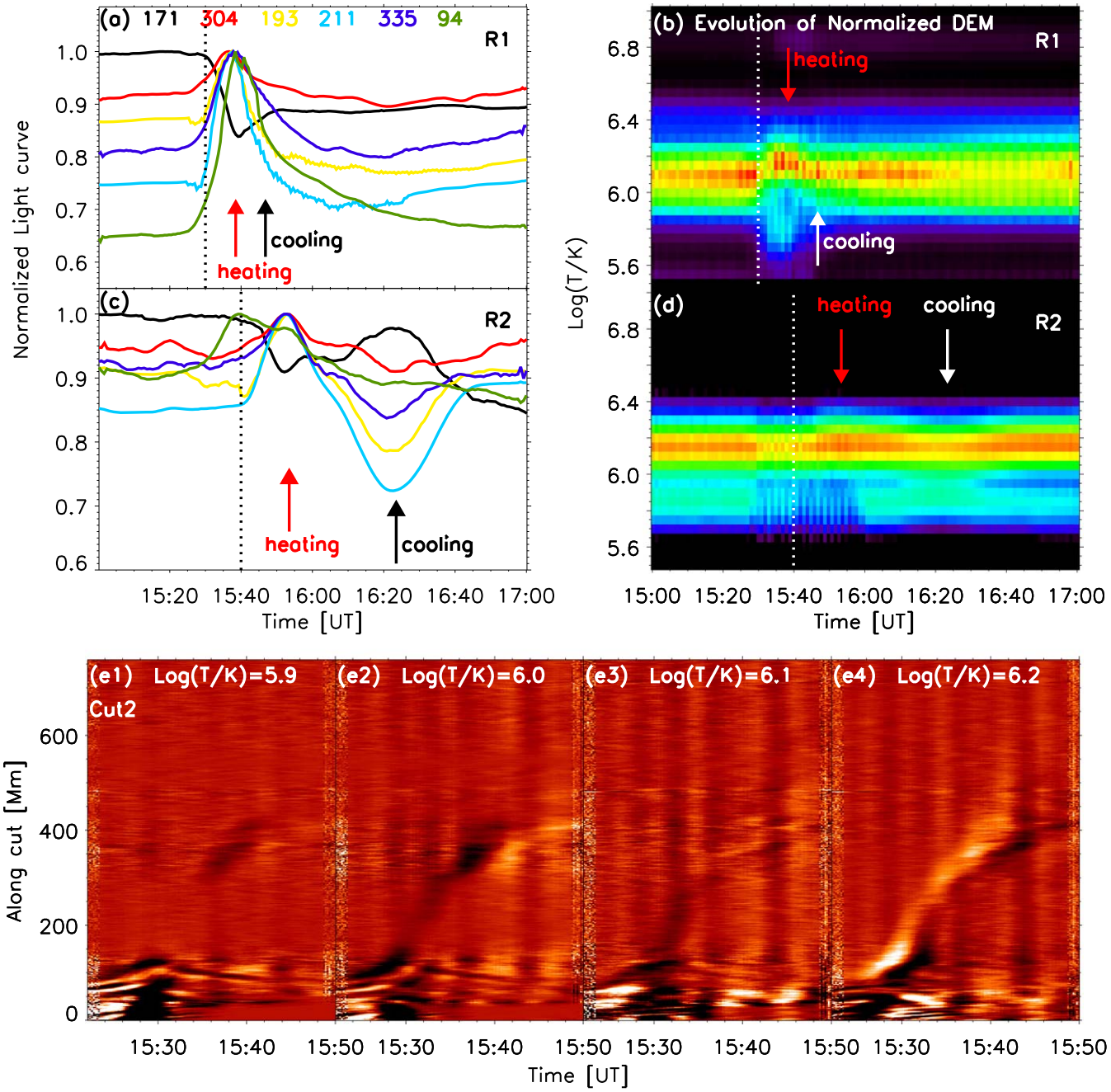

Figure 7. Temperature change of the coronal plasma caused by the EUV wave. Panels (a) and (c) show the normalized intensity variations in the AIA EUV passbands for regions "R1" and "R2", respectively. Panels (b) and (d) present the temporal evolution of the DEM for regions "R1" and "R2", respectively. The red and black arrows indicate the plasma heating and cooling phases, respectively. The vertical dotted lines mark the times of EUV wave passage. Panels (e1)–(e4) show the time-distance diagrams along Cut 2 from the running-difference DEM maps at four temperatures (i.e., $\log(T/K) = 5.9$, 6.0, 6.1, and 6.2).

5. Summary

In this study, we have presented the analysis results of a remarkable global EUV wave and its chromospheric counterpart the Moreton-Ramsey Wave with stereoscopic observations from SDO/AIA, STEREO-Ahead/EUVI, FY-3E/X-EUVI, and GONG. The EUV wave is associated with an X1.0 flare and a halo CME, and appears in the Hα and EUV passbands with different characteristic temperatures (e.g., 304 Å, 171 Å, and 193/195 Å).

The EUV wave becomes evident at a distance of ~150 Mm away from the eruption center and propagates circularly outward with an initial velocity of 600–720 km s^{-1} and a significant deceleration of 110–320 m s^{-2}. During the propagation of the EUV wave, the wave front propagates forwardly inclined to the solar surface with a tilt angle of ~53°.2. This implies that the propagating wave front is likely a dome-like structure, which could interact with the solar atmosphere. The plasma in the low corona is heated from $\log(T/K) \approx 5.9$ to $\log(T/K) \approx 6.2$ on the propagation path of the wave front. The 304 Å and Hα passbands also reveal signatures of the wave, indicating that the EUV wave could affect the low atmosphere. This event is also accompanied by a dimming region, which just follows the wave front and evolves from a small region to a ring-shaped region stopping at a distance of <150 Mm away from the eruption center. Our results suggest that the observed

EUV wave is likely a fast-mode MHD wave or shock driven by the expansion of its associated CME.

This work was supported by National Key R&D Program of China No. 2021YFA0718600, NSFC grants 11825301, 41931073, 41774195, and 11790304, Ten-thousand Talents Program of Jing-Song Wang, China Postdoctoral Science Foundation (grant numbers 2021M700246 and 2020M680201), and National Postdoctoral Program for Innovative Talents (BX20200013). AIA is an instrument on board the Solar Dynamics Observatory (SDO), a mission for NASA's Living With a Star program. We thank the SDO/AIA, FY-3E/X-EUVI, STEREO/SECCHI, and GONG for providing data.

ORCID iDs

Zhenyong Hou https://orcid.org/0000-0003-4804-5673
Hui Tian https://orcid.org/0000-0002-1369-1758
Qiao Song https://orcid.org/0000-0003-3568-445X
Ruisheng Zheng https://orcid.org/0000-0002-2734-8969
Hechao Chen https://orcid.org/0000-0001-7866-4358
Xianyong Bai https://orcid.org/0000-0003-2686-9153
Yajie Chen https://orcid.org/0000-0001-5494-4339

References

Asai, A., Ishii, T. T., Isobe, H., et al. 2012, ApJL, 745, L18
Biesecker, D. A., Myers, D. C., Thompson, B. J., Hammer, D. M., & Vourlidas, A. 2002, ApJ, 569, 1009
Chen, P. F. 2016, Geophysical Monograph Series, 216 (Washington DC: American Geophysical Union), 381
Chen, P. F., Fang, C., & Shibata, K. 2005, ApJ, 622, 1202
Chen, P. F., Wu, S. T., Shibata, K., & Fang, C. 2002, ApJL, 572, L99
Chen, P. F., & Wu, Y. 2011, ApJL, 732, L20
Cheung, M. C. M., Boerner, P., Schrijver, C. J., et al. 2015, ApJ, 807, 143
Delaboudinière, J. P., Artzner, G. E., Brunaud, J., et al. 1995, SoPh, 162, 291
Downs, C., Roussev, I. I., van der Holst, B., Lugaz, N., & Sokolov, I. V. 2012, ApJ, 750, 134
Downs, C., Warmuth, A., Long, D. M., et al. 2021, ApJ, 911, 118
Duan, Y., Shen, Y., Zhou, X., et al. 2022, ApJL, 926, L39
Eto, S., Isobe, H., Narukage, N., et al. 2002, PASJ, 54, 481
Gopalswamy, N., Nitta, N., Akiyama, S., Mäkelä, P., & Yashiro, S. 2012, ApJ, 744, 72
Harvey, J. W., Bolding, J., Clark, R., et al. 2011, AAS Meeting, 42, 17.45
Howard, R. A., Moses, J. D., Vourlidas, A., et al. 2008, SSRv, 136, 67
Hudson, H. S., Khan, J. I., Lemen, J. R., Nitta, N. V., & Uchida, Y. 2003, SoPh, 212, 121
Kaiser, M. L., Kucera, T. A., Davila, J. M., et al. 2008, SSRv, 136, 5
Kienreich, I. W., Temmer, M., & Veronig, A. M. 2009, ApJL, 703, L118
Lemen, J. R., Title, A. M., Akin, D. J., et al. 2012, SoPh, 275, 17
Li, T., Zhang, J., Yang, S., & Liu, W. 2012, ApJ, 746, 13
Liu, W., Jin, M., Downs, C., et al. 2018, ApJL, 864, L24
Liu, W., Nitta, N. V., Schrijver, C. J., Title, A. M., & Tarbell, T. D. 2010, ApJL, 723, L53
Liu, W., & Ofman, L. 2014, SoPh, 289, 3233
Liu, W., Ofman, L., Nitta, N. V., et al. 2012, ApJ, 753, 52
Long, D. M., DeLuca, E. E., & Gallagher, P. T. 2011, ApJL, 741, L21
Long, D. M., Jenkins, J., & Valori, G. 2019, ApJ, 882, 90
Moreton, G. E. 1960, AJ, 65, 494
Moreton, G. E., & Ramsey, H. E. 1960, PASP, 72, 357
Moses, D., Clette, F., Delaboudinière, J. P., et al. 1997, SoPh, 175, 571
Muhr, N., Veronig, A. M., Kienreich, I. W., et al. 2014, SoPh, 289, 4563
Nitta, N. V., Schrijver, C. J., Title, A. M., & Liu, W. 2013, ApJ, 776, 58
O'Dwyer, B., Del Zanna, G., Mason, H. E., Weber, M. A., & Tripathi, D. 2010, A&A, 521, A21
Ofman, L., & Thompson, B. J. 2002, ApJ, 574, 440
Okamoto, T. J., Nakai, H., Keiyama, A., et al. 2004, ApJ, 608, 1124
Olmedo, O., Vourlidas, A., Zhang, J., & Cheng, X. 2012, ApJ, 756, 143
Patsourakos, S., & Vourlidas, A. 2009, ApJL, 700, L182
Patsourakos, S., Vourlidas, A., Wang, Y. M., Stenborg, G., & Thernisien, A. 2009, SoPh, 259, 49
Pesnell, W. D., Thompson, B. J., & Chamberlin, P. C. 2012, SoPh, 275, 3
Samanta, T., Tian, H., Chen, B., et al. 2021, Innov, 2, 100083
Selwa, M., Poedts, S., & DeVore, C. R. 2012, ApJL, 747, L21
Shen, Y., Chen, P. F., Liu, Y. D., et al. 2019, ApJ, 873, 22
Shen, Y., Ichimoto, K., Ishii, T. T., et al. 2014a, ApJ, 786, 151
Shen, Y., & Liu, Y. 2012a, ApJL, 752, L23
Shen, Y., & Liu, Y. 2012b, ApJ, 754, 7
Shen, Y., Liu, Y., Su, J., et al. 2013, ApJL, 773, L33
Shen, Y., Liu, Y., Tian, Z., & Qu, Z. 2017, ApJ, 851, 101
Shen, Y., Liu, Y. D., Chen, P. F., & Ichimoto, K. 2014b, ApJ, 795, 130
Shen, Y., Tang, Z., Miao, Y., Su, J., & Liu, Y. 2018, ApJL, 860, L8
Shen, Y., Zhou, X., Duan, Y., et al. 2022, SoPh, 297, 20
Shibata, K., Kitai, R., Ueno, S., et al. 2011, Solar Activity in 1992-2003: Solar Cycle 23 Observed by Flare Monitoring Telescope (Kyoto: Kyoto Univ. Press)
Smith, S. F., & Harvey, K. L. 1971, in Observational Effects of Flare-Associated Waves, ed. C. J. Macris, 27 (Dordrecht: Reidel), 156
Su, Y., Veronig, A. M., Hannah, I. G., et al. 2018, ApJL, 856, L17
Thompson, B. J., Gurman, J. B., Neupert, W. M., et al. 1999, ApJL, 517, L151
Thompson, B. J., & Myers, D. C. 2009, ApJS, 183, 225
Thompson, B. J., Plunkett, S. P., Gurman, J. B., et al. 1998, GeoRL, 25, 2465
Thompson, B. J., Reynolds, B., Aurass, H., et al. 2000, SoPh, 193, 161
Tian, H., McIntosh, S. W., Xia, L., He, J., & Wang, X. 2012, ApJ, 748, 106
Veronig, A. M., Gömöry, P., Kienreich, I. W., et al. 2011, ApJL, 743, L10
Veronig, A. M., Muhr, N., Kienreich, I. W., Temmer, M., & Vršnak, B. 2010, ApJL, 716, L57
Veronig, A. M., Temmer, M., & Vršnak, B. 2008, ApJL, 681, L113
Vršnak, B., Magdalenić, J., Temmer, M., et al. 2005, ApJL, 625, L67
Vršnak, B., Warmuth, A., Brajša, R., & Hanslmeier, A. 2002, A&A, 394, 299
Wang, Y. M. 2000, ApJL, 543, L89
Warmuth, A., & Mann, G. 2005, A&A, 435, 1123
Warmuth, A., & Mann, G. 2011, A&A, 532, A151
Warmuth, A., Vršnak, B., Aurass, H., & Hanslmeier, A. 2001, ApJL, 560, L105
Wills-Davey, M. J., & Thompson, B. J. 1999, SoPh, 190, 467
Xue, J., Su, Y., Li, H., & Zhao, X. 2020, ApJ, 898, 88
Yang, L., Zhang, J., Liu, W., Li, T., & Shen, Y. 2013, ApJ, 775, 39
Ying, B., Feng, L., Lu, L., et al. 2018, ApJ, 856, 24
Zhang, P., Hu, X., Lu, Q., et al. 2021, AdAtS, 39, 1
Zheng, R., Jiang, Y., Hong, J., et al. 2011, ApJL, 739, L39
Zheng, R., Jiang, Y., Yang, J., et al. 2012a, ApJ, 747, 67
Zheng, R., Jiang, Y., Yang, J., et al. 2012b, A&A, 541, A49
Zheng, R., Jiang, Y., Yang, J., et al. 2012c, ApJL, 753, L29
Zheng, R., Jiang, Y., Yang, J., et al. 2012d, ApJ, 753, 112
Zheng, R., Jiang, Y., Yang, J., et al. 2013a, ApJ, 764, 70
Zheng, R. S., Jiang, Y. C., Yang, J. Y., et al. 2013b, MNRAS, 431, 1359
Zhou, X., Shen, Y., Su, J., et al. 2021a, SoPh, 296, 169
Zhou, X., Shen, Y., Tang, Z., et al. 2021b, arXiv:2112.15098